JMEPEG (2008) 17:767–771
DOI: 10.1007/s11665-007-9190-4

1059-9495/$19.00

Different Behavior in Electron Beam Welding of 18 Ni Co-free Maraging Steels

Zheng-Fei Hu, De-Feng Mo, Chun-Xu Wang, Guo-Qiu He, and Cheng-Shu Chen

(Submitted April 5, 2007; in revised form November 19, 2007)

Microstructures of two different 18 Ni Co-free maraging specimens A and B and their electron beam (EB) weld joints were investigated comparatively by optical microscopy and scanning electron microscopy (SEM). It is shown that both of the steels are typical lath martensite; however, grain size of specimen A is about three times as large as that of specimen B. X-ray diffraction (XRD) reveals that the amount of the reverted austenitic phase in A is obviously less than that in B. Most of the austenite distributes in plate form along grain and lath boundaries while some of it distributes as fine particles within the matrix. The microstructural differences between the two specimens led to diverse behaviors in EB welding. The specimen A is weldable but B shows obvious welding defects of pits and burn-through holes in weld face. The welding microstructure exhibits a typical dendritic morphology, and the grains in the heat-affected zone recrystallized and grew because of high temperatures of welding EB. The weldablity of the examined materials is related to the microstructure characteristics that markedly affected thermal conduction performance.

Keywords defect, electron beam welding, maraging steel, microstructure

1. Introduction

In relation to conventional carbon-hardened steels, maraging steels are a class of ultra high-strength steels characterized by very little carbon contents [Ref 1, 2]. The high mechanical resistance of these steels is attained by the precipitation hardening mechanism during aging. The traditional maraging steel grades contain about 8-12% cobalt in addition to other alloying elements. The 18 Ni Co-free maraging steels were developed by Inco Alloys Internatonal [Ref 3] in early 1980 due to a sharp rise in cobalt pricing in the late 1970s. As a result, maraging steels are important candidate materials for several critical applications such as rocket motor cases, cryogenic missiles and landing gears. For many of these applications, welding is an important means of fabrication. Electron beam (EB) welding is a process which produces coalescence of metals with extremely high-beam power density (about 10^5-10^7 W/cm^2) and has tremendous penetrating characteristics, with lower heat input, high-velocity, and the heat-affected zone is much smaller than that of any arc welding process. It is suitable for low-carbon steels like maraging steels. Therefore many research studies have been done on EB welding of 18 Ni Co-free maraging steels [Ref 4-6], but less attention was paid to weld defects such as pits and burn-through holes in weld face.

In the current work, the material of 18Ni Co-free maraging steel in the form of 2-mm-thick sheets was received in the same heat treatment condition: 850 °C1 h solution-annealed and 480 °C4 h aging. The two specimens were prepared from two batches with the same nominal composition Fe-18Ni-3.0Mo-1.4Ti. Microstructures of the base materials and the weld joints were examined. Special attention was paid to the weldability and weld defects of the examined materials.

2. Experimental Work

The chemical compositions of the examined 18 Ni Co-free maraging specimens are given in Table 1. It is shown that both of the specimens have similar chemical compositions. Two specimens were EB welded with the same welding parameters but their weldability exhibits different characteristics. One of the specimens, recognized as A (Fig. 1a), is weldable, its weld joint structure exhibits integrity from the top surface; while the other, recognized as B (Fig. 1b), has obvious welding defects of pits and burn-through holes in weld face. The corresponding microstructure is investigated in the following section.

Optical microscopy and scanning electron microscopy (SEM) were employed to observe the microstructures of base materials and their weld joints. Both the longitudinal (L-B) and transverse (B-T) sections of the weld joints were etched and examined, and the etchant used was: 100 ml H_2O, 8 g $(NO_2)_2C_6H_2OH$ (Picric acid), 5 ml H_2SO_4, 105 ml H_2O_2, and four drops of HF. X-ray diffraction (XRD) analysis was carried out on base materials without etchant to reveal the phases. XRD was carried out using step scan mode with step size of 0.02, time per step of 3 s and angular interval 62°-92°. Radiation CuKα (1.54056 A) was used with 40 kV and 100 mA.

Zheng-Fei Hu, De-Feng Mo, Guo-Qiu He, and **Cheng-Shu Chen**, School of Materials Science and Engineering, Tongji University, Shanghai 200092, China; and **Chun-Xu Wang**, Central Iron and Steel Research Institute, Beijing 100081, China. Contact e-mail: huzhengf@mail.tongji.edu.cn.

3. Results and Discussion

3.1 Base Materials

The microstructures of the base materials A and B are shown in Fig. 2. The grain size of A is much larger than that of B, about 10-20 μm and 3-6 μm, respectively. Besides the grain boundaries, the grains consist of randomly dispersed precipitates and bundles of parallel sub-grain boundaries that can be easily seen from Fig. 2(a) in the same etched condition.

Scanning electron microscopy observation from Fig. 3 indicates that the microstructures of the two materials are lath martensite. From the figures, the grain size of B is remarkably smaller than that of A, which corresponds to the results of optical microscopy. Quite a significant amount of reverted austenite distributes along grain and lath boundaries, and the preferential distribution is affected by alloy-rich segregations during aging [Ref 7]. In addition, a small amount of austenite appears as fine particles within the matrix of A, while much less particles are observed in B, which indicates that the austenite particles in specimen B concentrated in grain boundaries much heavily. A visual representation of information from Fig. 3(a) and (b) shows that the content of austenite especially that distributes along the grain boundaries of B is higher than that of A.

Table 1 The main chemical composition and impurity in examined sample (wt.%)

Specimen	Ni	Mo	Ti	C	S	P
A	18.35	2.89	1.42	0.005	0.001	0.005
B	19.10	2.70	1.36	0.003	0.003	0.004

It is interesting to note that the austenite in grain boundaries exhibits the appearance of granular instead of plate-like which was reported previously [Ref 8]; this is mainly due to the different etchant that was used. It demonstrates that different etchants lead to different appearances of reverted austenite.

Figure 4 shows the XRD comparison between two materials. The peaks of $(200)_\alpha$, $(211)_\alpha$ and $(220)_\gamma$ can be easily seen from diffraction diagrams, whereas the peaks of intermetallic phase, such as Ni_3Ti, Fe_2Mo, Ni_3Mo are not present, probably because their contents were too low. The austenite content was obtained by the direct comparison method. Quantitative analysis by XRD is based on the intensity of diffraction pattern of austenite or martensite phases in the samples. Without considering carbides, we can obtain the basic equation relating the diffracted intensities and the austenite volume fraction (C_γ) by the direct comparison method in an alloy containing only two phases [Ref 9]:

$$C_\gamma = \frac{1}{\frac{I_\alpha \cdot K_\gamma}{I_\gamma \cdot K_\alpha} + 1} \quad \text{(Eq 1)}$$

Here I_α and I_γ are pattern intensity of martensite and austenite given from XRD results; and K_α and K_γ are their reflection ability, respectively, which can be calculated with crystal structure and other correlative parameters.

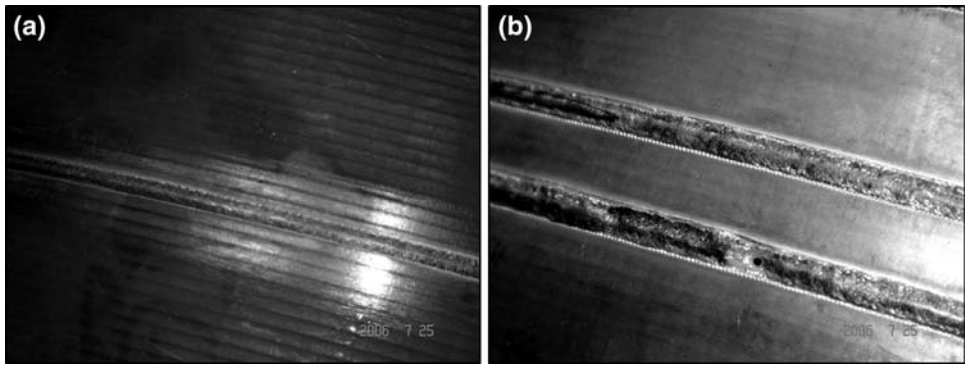

Fig. 1 Appearances of the welding seam. (a) Specimen A and (b) specimen B

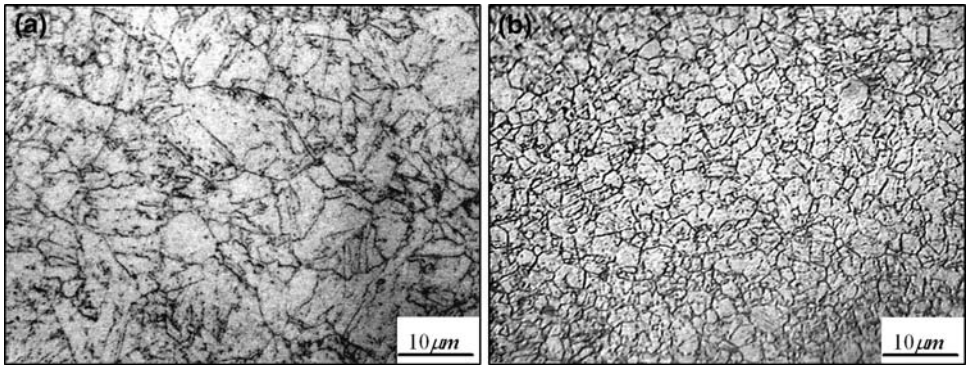

Fig. 2 Optical micrographs of base materials. (a) Specimen A and (b) specimen B

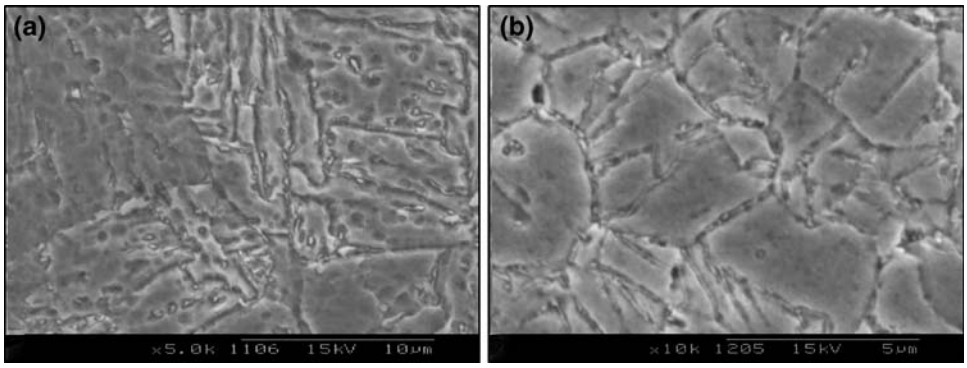

Fig. 3 SEM micrographs of the base materials. (a) Specimen A and (b) specimen B

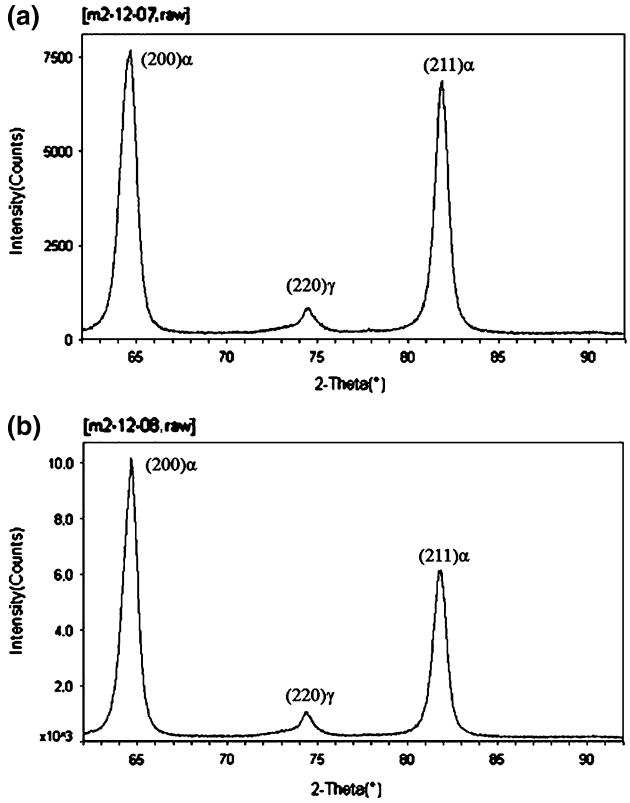

Fig. 4 XRD of the base materials. (a) Specimen A and (b) specimen B

In the present case, $(220)_\gamma$was compared with $(200)_\alpha$ and $(211)_\alpha$, the average value of two compared groups was calculated to minimize the effect of preferential direction, and the austenite content for specimen A and B are 6.8 and 9.6%, respectively.

3.2 Weld Joints

Figure 5 shows the microstructures of weld joints. The weld width especially at the bottom of B (Fig. 5b) is wider than that of A (Fig. 5a), which resulted in bigger welding area and larger quantity of molten metals during EB welding process. All welding microstructures of both A and B exhibit a typical dendritic morphology (Fig. 5c, d), and the growth direction of dendritic crystals is basically vertical to the welding direction (Fig. 5a, b). This is because in the high speed of EB welding, the rear part of molten pool is distorted to a tear-drop shape instead of an ellipse. The temperature in the center of welding seam was higher than 1,800 °C, while the weld width was about 2 mm, which resulted in the enormous gradients of temperature and provided the advantageous condition for the growth of dendritic crystals. However, differences in solidification morphology were also observed within the transverse (B-T) section of the weld metal. The grains in specimen A are cystiform-dendritic, which have well-developed secondary dendrites stretched from main dendrites (Fig. 5e), and many of them are in irregular cross shape. In specimen B, grains exhibit more circular microstructure with very few secondary dendrites present (Fig. 5f), presumably owing to the more rapid rate of temperature changing near the crystallization front in the latter specimen, which results in unfavorable growth conditions for secondary dendrites.

The heat-affected zones of the base materials were also examined by SEM. Nearly similar microstructures are seen in Fig. 6. The region adjoining the weld metal gets heated to high temperatures in the austenite phase field before cooling rapidly. Energy provided by EB welding was high enough to lead to grain recrystallization [Ref 10]. As in this case, crystal grains grew and the grain sizes of specimen A and B in this area are about 45μm and 35μm, respectively, which are 2 and 6 times larger than that before EB welding. The grain boundaries near weld junction exhibit grooving, which is easily seen in Fig. 6(a). It is believed that the presence of inclusions in maraging steel weldments liquified locally in impurity-rich regions and the grain boundaries were markedly attacked by the etchant [Ref 6].

3.3 Analysis on Weld Defects

Both the specimens A and B are 18 Ni Co-free maraging steels with the same nominal chemical composition and EB welded with the same welding parameters. However, the weld joints of specimen B get burn-through problem. An explanation is offered in terms of different forces on molten pool in the process of EB welding. Figure 7 shows the forces on molten pool before the weld defects appear.

In Fig. 7, f_G is the pressure duo to gravity of melting metals, f_E is stress of high-energy EB and f_S is surface tension of molten pool. The value of f_G depends on quantity of molten metal during EB welding, f_E depends on welding voltage and current, and f_S can be determined by the category of metal and the surface condition of molten pool. Besides, the adsorption

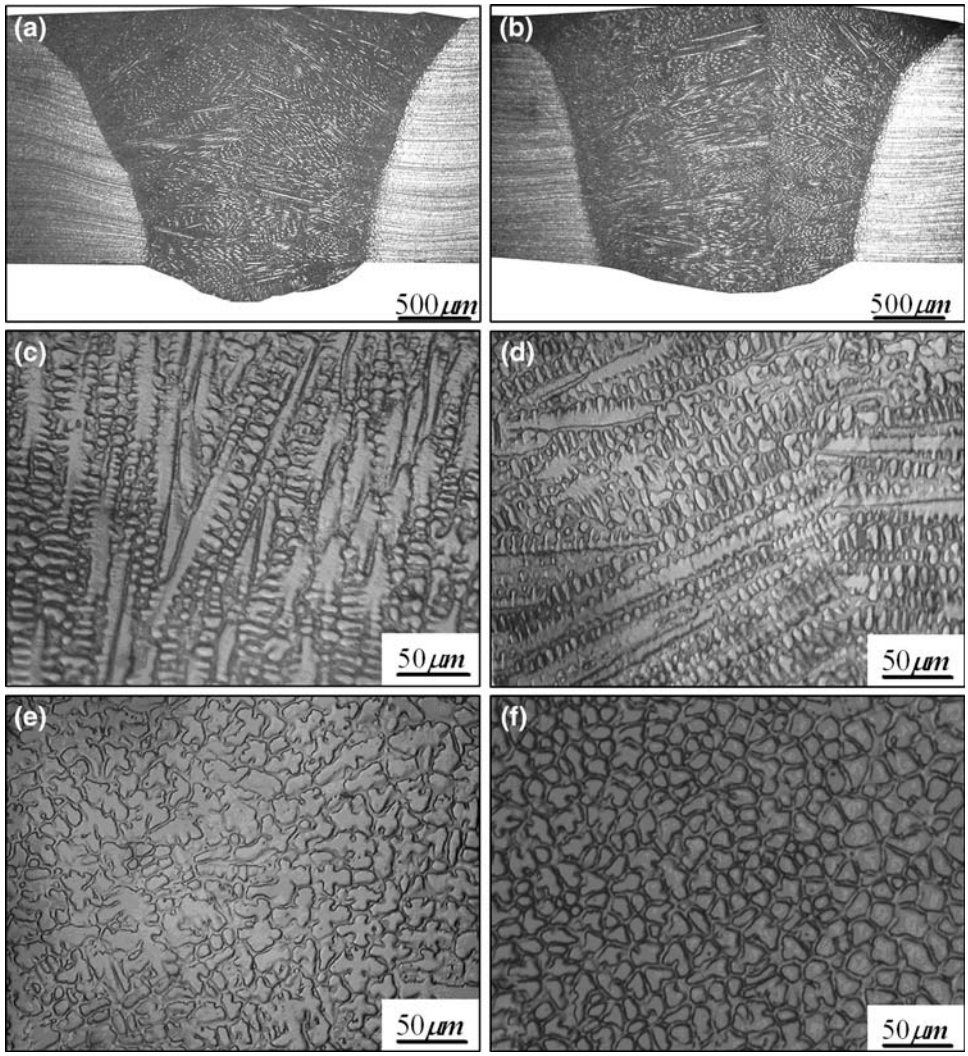

Fig. 5 Optical micrographs of weld joints. (a) and (b) Weld seam of specimen A and B (L-B section); (c) and (d) Fusion zone of specimen A and B (L-B section); and (e) and (f) Fusion zone of specimen A and B (B-T section), respectively

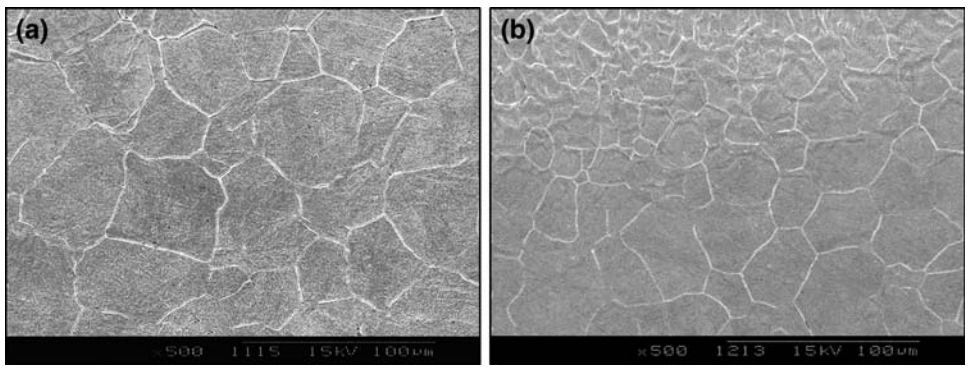

Fig. 6 SEM micrographs of the heat-affected zones near weld junction (L-B section). (a) specimen A and (b) specimen B

between solid and liquid state and the cohesion in molten metal have a negligible contribution in keeping the stability of molten pool from burn-through [Ref 11]. Obviously, f_G and f_E are the main forces that lead to weld penetration, while f_S gives a negative force. When f_S cannot counteract the composition forces of f_G and f_E, weld defects arise.

In this study, EB welding was carried out without filler, the metals in molten pool have the same chemical composition as base materials. Therefore, the microstructures of the two materials with different composing phases and their relative contents have distinct contributions to thermal conduction performance, which resulted in diverse heat accumulation and

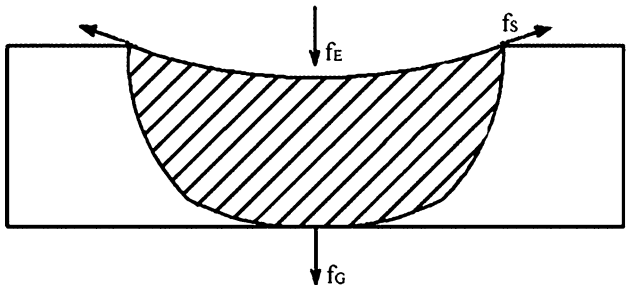

Fig. 7 The force on molten pool

quantity of melting metals, and have a great influence on weldability.

For 18 Ni Co-free maraging steel, electron heat conduction is a dominant mechanism of heat transport. Comparing specimen A with B, the contrast of grain size is remarkable; the grain size of specimen A is about two times bigger than that of B in base materials, and the grain size is also bigger in heat-affected zones when the grains recrystallize. Because of the smaller grain size, specimen B has more grain boundaries, which scatter electrons more strongly, and this inhibits heat conduction. In addition, there is larger quantity of reverted austenite in specimen B, especially in grain boundaries. Unfortunately, the thermal conductivity of austenite is poorer than that of martensite [Ref 12]. As discussed above, grain boundaries and reverted austenite are weak link to heat conduction, which makes a poorer thermal conductivity of specimen B than that of A.

From the longitudinal (L-B) section of molten pool, specimen B shows a larger welding area, which illustrates specimen B has more quantity of molten metals during EB welding process and an increasing value of f_G. Besides, from the microstructure of weld joints in transverse (B-T) section, the temperature gradient in the area near the crystallization edge of specimen B must be greater than that of specimen A, which is consistent with the above conclusion of poorer thermal conductivity of specimen B. During EB welding, the temperature in the region adjoining the weld metal was nearly the same in two specimens, and approached fusion point. Specimen B had a greater temperature gradient and a wider weld width, which led to distinct heat accumulation and larger value of f_G than that in specimen A. Meanwhile, with the increase of molten metal, the width at the bottom of molten pool increased, the weld line tended to become parallel to the direction of thickness and shortened, and the f_S decreased. The stress f_E remained constant in the same welding condition. As a result, the value of f_G plus f_E exceeded f_S, and burn-through problems happened. Because of poor thermal conduction performance in specimen B, the energy input should be reduced when EB welding in contrast with specimen A, which could give advantageous effect to avoid the welding defects.

4. Conclusions

(1) The microstructure of the two 18 Ni Co-free maraging steels investigated in the study is lath martensite. The austenite distributes in plate form along granular and lath boundaries while some as fine particles within the matrix. Compared with specimen B, the grain size of specimen A is about two times bigger and has much less content of reverted austenite.

(2) All welding microstructures of both specimen A and B exhibit a typical dendritic morphology. However, the microstructure of specimen A weld in transverse (B-T) section is cystiform-dendritic with well-developed secondary dendrites, while B exhibits a more circular microstructure with few secondary dendrites. Compared with the change in specimen A, the grains near weld junction in specimen B recrystallized and grew markedly.

(3) In comparing the weldability of the two materials, it is noted that welding defects of burn through are contributed greatly by small grain size and high volume of austenite content, which induces poor thermal conduction performance.

References

1. R.F. Decker, *Source Book on Maraging Steels: A Comprehensive Collection of Outstanding Articles from the Periodical and Reference Literature*. American Society for Metals, Metals Park, ON, 1979
2. F. Ayman, M. Taha, and E.F. Hoda, et al., Mechanical Properties of New Low-Nickel Cobalt-Free Maraging Steels, *Steel Res.*, 2002, **73**(12), p 549–556
3. L.W. Tsay, W.B. Huang, and C. Chen, Gaseous Hydrogen Embrittlement of T-250 Laser Welds, *J. Mater. Eng. Perform.*, 1997, **6**(2), p 182–186
4. X.F. Chen, J.H. Li, and Z.K. Li, et al., Study on Local Heat Transfer of 18Ni Maraging Steel After Electron Beam Welding, *Steel Res.*, 1994, **65**(12), p 557–560
5. R.K. Prasad and P.V. Venkitakrishnan, Electron Beam Welding of M-250 Grade Maraging Steel, *Prakt. Metallogr.*, 1993, **30**(3), p 129–136
6. C.R. Shamantha, R. Narayanan, and K.J.L. Iyer, et al., Microstructural Changes During Welding and Subsequent Heat Treatment of 18Ni (250-Grade) Maraging Steel, *Mater. Sci. Eng. A*, 2000, **287**(1), p 43–51
7. X.D. Li and Z.D. Yin, Reverted Austenite During Aging in 18Ni (350) Maraging Steel, *Mater. Lett.*, 1995, **24**(4), p 239–242
8. R.F. Decker and S. Floreen, Maraging Steel-The First 30 Year, In: Maraging Steel Recent Development and Application. *Symposium of TMS Annural Meeting*, Phenix, Arizona, 1988, p 141–143
9. J.M. Pardal, S.S.M. Tavares, and M.P. Cindra Fonseca, et al., Study of the Austenite Quantification by X-ray Diffraction in the 18Ni-Co-Mo-Ti Maraging 300 Steel, *J. Mater. Sci.*, 2006, **41**(8), p 2301–2307
10. M.C. Coleman and M.F. Jordan, Fracture Toughness and Microstructure of the Heat-Affected Zone of a Welded Maraging Steel, *Metals Technol.*, 1974, **1**, p 24–30
11. Z.M. Xu, Application of TIG Welding with Stainless Steel Sheet, *Electric Welding Machine*, 2005, **35**(6), p 65–66
12. J.B. Xie, H.M. Cheng, and T.C. He, et al., Numerical Simulation of Temperature Field in Steel 1045 During Its Quenching, *J. Gansu Uni. Technol.*, 2003, **29**(4), p 33–37